

Toroidal Confinement and Beyond: Vorticity-Defined Morphologies of Dipolar ^{164}Dy Quantum Droplets

S. Sanjay^{1,*}, S. Saravana Veni^{1,†} and Boris A. Malomed^{2,3‡}

¹*Department of Physics, Amrita School of Physical Sciences,
Amrita Vishwa Vidyapeetham, Coimbatore-641112, Tamil Nadu, India.*

²*Department of Physical Electronics, School of Electrical Engineering,
Faculty of Engineering, Tel Aviv University, Tel Aviv 69978, Israel. and*

³*Instituto de Alta Investigación, Universidad de Tarapacá, Casilla 7D, Arica, Chile.*

We investigate the formation, stability, and dynamics of 3D ring-shaped and multipole vortical quantum droplets (QDs) in non-rotating dipolar Bose-Einstein condensates held in a toroidal trapping potential. The QD dynamics are investigated in the framework of the extended Gross-Pitaevskii equation, which includes long-range dipole-dipole interactions (DDI) and the beyond-mean-field Lee-Huang-Yang (LHY) term, revealing the emergence of self-bound states. Stable stationary solutions for multipole QDs with different values of the topological charge (vorticity S) are shaped as necklace-like modes, with the number of “beads” (multipole’s order) $n = 2S$, up to $S = 6$. The stability area of the multipoles shrinks with the increase of S . For higher values of S the centrifugal effect associated with the phase winding destabilizes the annular density and drives the formation of fragmented multipole droplet states. The dependence of the chemical potential, total energy and peak density on the norm (number of particles) and S is produced. These findings uncover the stabilizing effect of the LHY correction and DDI anisotropy in maintaining complex QD states in the non-rotating configurations.

I. INTRODUCTION

A great advancement has been achieved in recent studies of macroscopic quantum phenomena such as formation of quantum droplets (QDs) [1–3], supersolidity [4–6], vortices [7–9], and others. Specifically, the investigation of QDs, which are sustained by the stable balance between the mean-field (MF) interactions and beyond-MF [Lee-Huang-Yang (LHY)] corrections to them, induced by quantum fluctuations [10, 11], offers a broad framework for the development of these studies, owing to the relative simplicity of the theoretical model and their availability for the experiment [12, 13]. The so predicted QD stability within the MF-LHY framework aligns well with outcomes generated by the Monte Carlo method applied to the corresponding many-body setting [14–19].

In the experiment, QDs were initially created in Bose-Einstein condensates (BECs) of magnetic atoms [20, 21]. A great deal of interest has also been drawn to QDs, filled by ultra-diluted superfluids, in homonuclear [22, 23] and heteronuclear [24, 25] binary BECs with contact interatomic interactions. In the latter case, the formation of stable QDs is provided by the possibility to properly adjust the corresponding atomic collision length by dint of the Feshbach-resonance effect, imposed by the DC magnetic field [26]. In addition to the formation of QDs, also studied were collisions between moving QDs in one-dimensional (1D) [27], 2D [28], and 3D [29] geometries, along with the experimentally observed effectively 1D scattering of QDs on localized potentials [30]. On the other hand, the long-range dipole-dipole interactions

(DDI) in the BEC of magnetic atoms enable the realization of stable anisotropic QD configurations [31–35]. In particular, QD structures in 3D harmonic-oscillator (HO) and potential-box potentials have been studied [36, 37]. Ground-state and metastable striped patterns (superstripe states), trapped in the 3D HO potentials, were reported too [38]. Beyond the BEC realm, studies of droplet phenomena have been extended to vapors [39] and nonlinear photonic systems [40–42].

An obviously interesting but challenging possibility is the incorporation of vorticity into self-bound QDs. The self-interaction causes azimuthal instability, which tends to split the 3D vortex into fragments [43–45]. This issue can also be resolved with the help of the LHY corrections. The balance between the self-repulsive LHY terms and the MF attractive ones results in stable configurations, which is similar to the mechanism known in nonlinear optics, where the stability may be provided by the competitive cubic-quintic nonlinearity [46, 47]. Thus, stable 2D [48–50] and 3D [51] vortex QDs (VQDs) with the embedded angular momentum have been predicted, as summarized in Ref. [52]. Metastable ring-shaped QD clusters and rotating VQD clusters carrying multiple vorticity were predicted too [53, 54]. The VQD stability can be enhanced by trapping the BEC in a toroidal potential [55]. Toroidal traps are especially adept at accommodating vortex states due to their inherent rotational symmetry and ability to sustain persistent currents [56]. In particular, the formation of 3D stable vortices and multipole QDs (necklace-shaped chains) under the toroidal confinement were demonstrated up to vorticity of $S = 12$ [55]. In the absence of the trapping potential, VQDs with high topological charges require an enormous number of atoms to retain their stability [48, 51]. A similar mechanism ensures the stabilization of 2D VQDs with different vorticities [57, 58] and multipole 2D QDs [59] by means

* s.sanjay@cb.students.amrita.edu

† s.saravanaveni@cb.amrita.edu.in

‡ malomed@tauex.tau.ac.il

of the annular trap.

VQDs in dipolar BECs were studied too [60], where the long-range DDI is fundamentally different from the contact interactions in binary condensates. These studies further demonstrate that isotropic vortex solutions, with dipoles polarized parallel to the vortical axis, are inherently unstable. Stable VQDs have been predicted in 2D anisotropic dipolar configurations, with the dipoles polarized at an angle to the pivot [61]. Despite the significant progress in the studies of VQDs, multipole QDs in dipolar BEC trapped in the 3D toroidal geometries have not been addressed as yet, which is the objective of the present work. Experimentally, toroidal potentials have been employed to probe superfluid properties, such as the quantized circulation and stability thresholds of long-lived states [62, 63]. These ring-shaped traps support topologically nontrivial structures, including persistent currents [64, 65] and knotted vortex lines. They have also been proposed as platforms for exploring entanglement phenomena in expanding BECs [66]. Recent work [67] has predicted the formation of Josephson vortices in a stacked pair of toroidal BECs, in the framework of a dissipative Gross-Pitaevskii (GP) equations.

Motivated by the fact that the toroidal potentials, when combined with the repulsive LHY nonlinearity, enhances the robustness of the self-bound QDs, where the toroidal trap creates the localized-density states, and the self-repulsive LHY helps in stabilizing them. In the droplets carrying vorticity S , the centrifugal contribution to the kinetic energy, generated by the phase winding, which is proportional to S^2 , pushes the density outward and competes with the toroidal confinement and LHY repulsion. The competition leads to the spontaneous emergence of multipole droplet structures, which is the central result of the present work. The present work aims to systematically investigate structural characteristics and stability of ring-shaped and multipole QDs in the 3D dipolar BEC confined by the toroidal potential. Our numerical analysis combines the imaginary-time propagation (ITP) and real-time propagation methods, to produce both stationary and evolving solutions, focusing on their physically relevant characteristics, such as the chemical potential, peak density, radial and axial widths, and vortex-core structure, for different winding numbers (vorticity values). The paper is organized as follows: in Section II, we present the model for the dipolar BEC, which includes the MF and LHY interactions, along with the toroidal confinement. Section III is divided in three parts: III.1 addresses stationary states of multipole droplets under toroidal confinement, in III.2 we examine their stability under perturbations, and in III.3 we present the stationary states under the action of the Gaussian confinement. The paper is concluded by Section IV.

II. THE MODEL

The dipolar BEC composed of N atoms with mass m , whose magnetic moment is oriented along the z -axis, is

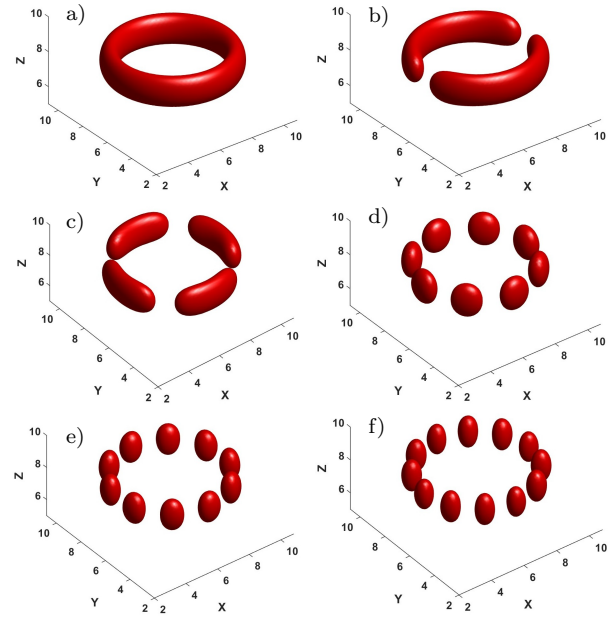


FIG. 1. Isosurface plots illustrating stable ring-shaped and multipole QD density profiles for different winding numbers S , with norm $N = 2000$, DDI length $a_{dd} = 130.8a_0$, scattering length $a = 100a_0$, and the coefficient of the LHY term $\gamma_{QF} = 2.697 \times 10^7 a_0^{5/2}$, confined in the toroidal potential (7). (a) The axisymmetric mode with $S = 0$. (b) A dipole QD configuration with $S = 1$. (c) A quadrupole QD with four density lobes for $S = 2$. The panels in the bottom row display stable higher-order multipole structures with 8, 10, and 12 density lobes, obtained for $S = 4$, $S = 5$, and $S = 6$, respectively. All the stationary states are obtained by means of the ITP method.

accurately modeled by the LHY-amended GP equation, which includes the contact interactions and DDI [68, 69]:

$$i\hbar \frac{\partial \psi(\mathbf{r}, t)}{\partial t} = \left[-\frac{\hbar^2}{2m} \nabla^2 + V(\mathbf{r}) + \frac{4\pi\hbar^2}{m} a N |\psi(\mathbf{r}, t)|^2 + \frac{3\hbar^2}{m} a_{dd} N \int V_{dd}(\mathbf{R}) |\psi(\mathbf{r}')|^2 d\mathbf{r}' + \frac{\gamma_{QF} \hbar^2 N^{3/2}}{m} |\psi(\mathbf{r}, t)|^3 \right] \psi(\mathbf{r}, t), \quad (1)$$

$$V_{dd}(\mathbf{R}) = \frac{1 - 3 \cos^2 \theta}{|\mathbf{R}|^3}, \quad \mathbf{R} = \mathbf{r} - \mathbf{r}', \quad a_{dd} = \frac{\mu_0 \mu^2 m}{12\pi\hbar^2}, \quad (2)$$

where ∇^2 is the 3D Laplacian, $V(\mathbf{r})$ is the external potential, a denotes the scattering length of the contact interaction and a_{dd} denotes the dipolar interaction length. Kernel V_{dd} determines long-range interaction between two magnetic atoms positioned at $\mathbf{r} = \{x, y, z\}$ and $\mathbf{r}' = \{x', y', z'\}$, where θ is the angle between vector \mathbf{R} and the z axis. The singularity introduced by the dipolar potential is taken care of by evaluating them in momentum space (k), where the momentum-space kernel was regularized using a spherical truncation method [70] and the $k = 0$ component was set to zero, avoiding the

singularity while preserving the long-range anisotropic character of the dipolar interaction. The wavefunction is normalized to $\int |\psi(\mathbf{r}, t)|^2 d\mathbf{r} = 1$. In the scaled form, the effective DDI length is $\epsilon_{dd} \equiv a_{dd}/a$. For the formation of QDs, we consider strongly dipolar atoms, with $a_{dd} > a$ (for $a_{dd} < a$, the system is effectively repulsive, causing decay of localized inputs). Taking the value of $a_{dd} = 130.8a_0$ [71] for ^{164}Dy atoms, where a_0 is the Bohr radius, there remains flexibility in determining the scattering length a , as it may be tuned by means of the Feshbach resonance [72]. Here, we set $a = 100a_0$. The coefficient of the LHY (alias quantum-fluctuation, QF) term [73–75] is

$$\gamma_{\text{QF}} = \frac{128}{3} \sqrt{\pi a^5} Q_l(\epsilon_{dd}), \quad (3)$$

with the auxiliary function [76]

$$Q_l(\epsilon_{dd}) = (1 - \epsilon_{dd})^{l/2} {}_2F_1\left(\frac{-l}{2}, \frac{1}{2}; \frac{3}{2}; \frac{3\epsilon_{dd}}{\epsilon_{dd} - 1}\right) \quad (4)$$

where ${}_2F_1\left(\frac{-l}{2}, \frac{1}{2}; \frac{3}{2}; \frac{3\epsilon_{dd}}{\epsilon_{dd} - 1}\right)$ is the hypergeometric function. Here, l is an integer, represents the order of the momentum-space integral in the Bogoliubov treatment of QF. Following [77], the effect of the DDI on the QF-induced energy correction is most significant for $l = 5$, which is therefore used in the evaluation of $Q_l(\epsilon_{dd})$ in our calculations, improving the prospects for experimental verification. In this case, Eq. (4) reduces to

$$Q_5(\epsilon_{dd}) \approx 1 + \frac{3}{2}\epsilon_{dd}^2 \quad (5)$$

[78]. We use the simplified expression of $Q_5(\epsilon_{dd})$ (Eq. (5)) in numerical simulations, for which $\gamma_{\text{QF}} = 2.697 \times 10^7 a_0^{5/2}$. The scaled form of Eq. (1) is produced by measuring lengths in units of $l_0 = \sqrt{\hbar/m\omega_0}$, time and energy in units of $t_0 = \omega_0^{-1}$ and $\hbar\omega_0$, respectively, and density $|\psi|^2$ in units of l^{-3} (here ω_0 is the reference angular frequency, introduced for the nondimensionalization of the GP equation; it is not a frequency imposed by the toroidal trapping potential in Eq. (7)) :

$$\begin{aligned} i \frac{\partial \psi(\mathbf{r}, t)}{\partial t} = & \left[-\frac{1}{2} \nabla^2 + V(\mathbf{r}) + 4\pi a N |\psi(\mathbf{r}, t)|^2 \right. \\ & + 3a_{dd} N \int \frac{1 - 3 \cos^2 \theta}{|\mathbf{R}|^3} |\psi(\mathbf{r}')|^2 d\mathbf{r}' \\ & \left. + \gamma_{\text{QF}} N^{3/2} |\psi(\mathbf{r}, t)|^3 \right] \psi(\mathbf{r}, t). \end{aligned} \quad (6)$$

We here adopt the natural form of the toroidal trapping potential, which is available in the experiment [79, 80]:

$$\begin{aligned} V(\mathbf{r}) = & -p \exp \left[-\frac{(\rho - \rho_0)^2}{d^2} - \frac{z^2}{z_0^2} \right], \\ \rho \equiv & \sqrt{x^2 + y^2}, \end{aligned} \quad (7)$$

where coefficients p and ρ_0 , d , z_0 define the potential depth, and obvious geometric parameters, respectively.

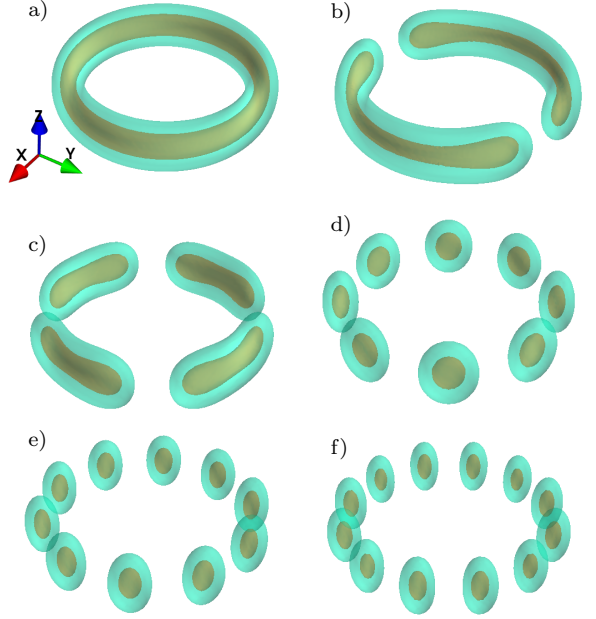


FIG. 2. The magnified view of the density distribution in the stable stationary ring-shaped and multipole QDs in the absence of the LHY correction, $\gamma_{\text{QF}} = 0$, for different vorticities. Results are shown for $N = 5000$ atoms with DDI length $a_{dd} = 130.8a_0$ and scattering length $a = 100a_0$, confined in the toroidal potential (7). Panels correspond to: (a) $S = 0$, (b) $S = 1$, (c) $S = 2$, (d) $S = 4$, (e) $S = 5$, and (f) $S = 6$. The plots display the spatial localization and symmetry of the stable QDs. The stationary states are obtained by means of the ITP method.

Here, p is expressed in terms of $\hbar\omega_0$. The mass of ^{164}Dy atoms is $m = 164 \times 1.66054 \times 10^{-27}$ kg. With the reference frequency $\omega_0 = 2\pi \times 61$ Hz, the characteristic length and time are $l_0 = \sqrt{\hbar/m\omega_0} \equiv 1.01 \mu\text{m}$ and $t_0 = \omega_0^{-1} \equiv 2.61$ ms. Further, ρ_0 , d , z_0 are expressed in terms of the above scaling parameter l_0 . Expanding Eq. (7) around its minimum ($\rho = \rho_0$, $z = 0$), yields the following values of the second derivatives

$$V''(\rho_0) = \frac{2p}{d^2}, \quad V''(0) = \frac{2p}{z_0^2}. \quad (8)$$

For the trap parameters $p = 4$, $\rho_0 = 2\pi$, $d = \sqrt{6}$, and $z_0 = \sqrt{6}$, we thus obtain $V''(\rho_0) = V''(0) = 4/3$, hence the effective radial and axial trapping frequencies (in units of ω_0) are

$$\Omega_\rho = \Omega_z = \Omega = \sqrt{4/3}.$$

Using the reference frequency $\omega_0 = 2\pi \times 61$ Hz, the respective physical-trap frequencies are $f_\rho = f_z = \Omega \times (\omega_0/2\pi) \simeq 70.43$ Hz. Unless stated otherwise, the numerical results are presented using the above-mentioned trapping parameters, which adequately represent the generic case (simulations performed with other parameters produced similar results). The study of multipole QDs is carried out by varying atom number N and the vorticity S (the topological charge, alias the winding number),

while fixing the DDI length $a_{dd} = 130.8a_0$, the scattering length of the contact interaction $a = 100a_0$, and the LHY coefficient $\gamma_{QF} = 2.697 \times 10^7 a_0^{5/2}$. The scaled equation (6) keeps the unitary normalization, i.e.,

$$\int \int \int |\psi|^2 dx dy dz = 1. \quad (9)$$

Using the variational principle, Eq. (1) can be written as

$$i \frac{\partial \psi}{\partial t} = \frac{\delta E}{\delta \psi^*}, \quad (10)$$

where $\delta/\delta\psi^*$ is the variational derivative, and the system's energy is

$$\begin{aligned} E = & \int d\mathbf{r} \left[\frac{1}{2} |\nabla \psi(\mathbf{r})|^2 + V(r) |\psi(\mathbf{r})|^2 + 2\pi N a |\psi(\mathbf{r})|^4 \right. \\ & + \frac{3}{2} a_{dd} N |\psi(\mathbf{r})|^2 \int \frac{1 - 3 \cos^2 \theta}{|\mathbf{R}'|^3} |\psi(\mathbf{r}')|^2 d\mathbf{r}' \\ & \left. + \frac{2\gamma_{QF}}{5} N^{3/2} |\psi(\mathbf{r})|^5 \right]. \end{aligned} \quad (11)$$

III. NUMERICAL RESULTS

The integrodifferential GP equation Eq. (6) was solved numerically using the split-time-step Crank-Nicolson algorithm, adapting the FORTRAN/C programs [81] or their open-multiprocessing versions [82]. In particular, stationary solutions were obtained by means of the ITP method. This was performed with nearly equal discretization steps in the x , y , and z directions.

Droplets confined in the toroidal potential resemble lifebelts (or “donuts”). We address VQDs solutions with the vorticity up to $S = 12$. The trapping toroidal potential significantly constrains the VQDs, unlike the characteristic flat-top profiles of free-space VQDs and vortex solitons [48, 85]. To enable the numerical investigation of the VQDs states, we use the input shaped as the phase-imprinted Gaussian states [83]:

$$\psi(x, y, z) \propto (x + i y)^S \exp \left(-\frac{\rho^2}{\delta_r^2} - \frac{z^2}{\delta_z^2} \right), \quad (12)$$

where $\rho^2 = x^2 + y^2$. The phase of this complex expression is $\Phi = S \arctan(y, x)$. δ_r and δ_z are the width parameters, we set $\delta_r = \delta_z \equiv \sqrt{2}$ for the numerical calculation.

III.1. Stationary states of multipole droplets under toroidal confinement

The interplay of the toroidal confinement, represented by Eq. (7), with the local and nonlocal interactions included in Eq. (6) leads to diverse morphologies of the VQDs. Naturally, multipole droplets tend to form with

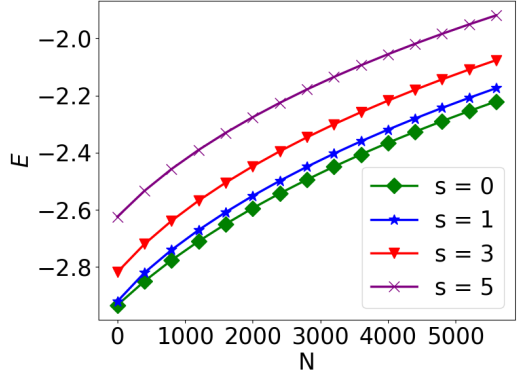


FIG. 3. Total energy E as a function of atom number N for different vorticities S in the absence of the LHY correction ($\gamma_{QF} = 0$), the dipolar and scattering lengths being $a_{dd} = 130.8a_0$ and $a = 100a_0$. The stationary states are produced by means of ITP. With the increase of N , the energy increases monotonously for given values of S . The $S = 0$ configuration yields the lowest energy, corresponding to the ground state, while the branches with $S = 1, 3, 5$ correspond to multipole excited states.

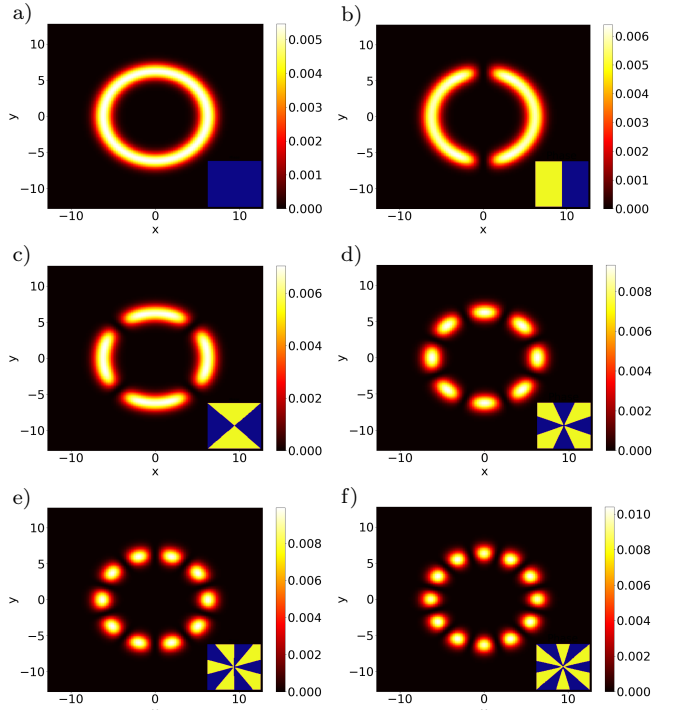


FIG. 4. Contour plots of the 2D density projection in the (x, y) plane, corresponding to the stable stationary isosurface profiles, shown in Fig. 1, for $N = 2000$, $a_{dd} = 130.8a_0$, $a = 100a_0$, $\gamma_{QF} = 2.697 \times 10^7 a_0^{5/2}$ and for different vorticities S : (a) $S = 0$, (b) $S = 1$, (c) $S = 2$, (d) $S = 4$, (e) $S = 5$, and (f) $S = 6$. The inset in each panel shows the corresponding phase profile, which reveals the topological structure and phase singularities of each state. All stationary configurations were produced by means of the ITP method.

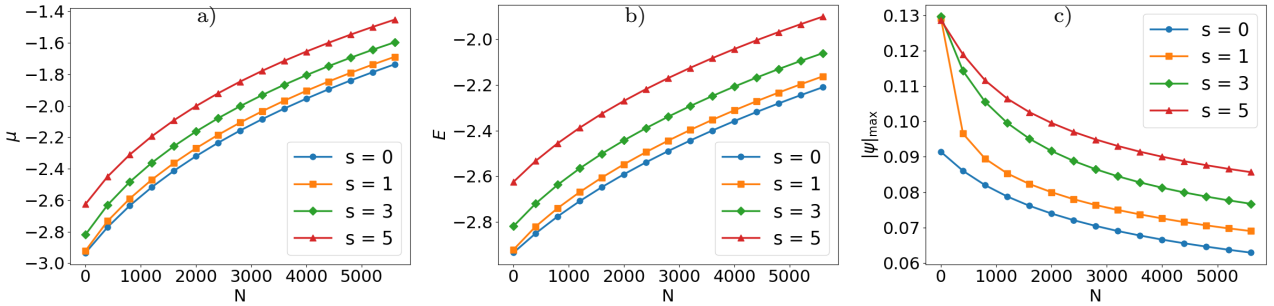


FIG. 5. a) The chemical potential μ , (b) the total energy E , and (c) amplitude ψ_{\max} vs. the number of atoms N in stationary QD states with DDI length $a_{\text{dd}} = 130.8a_0$, scattering length $a = 100a_0$, and LHY coefficient $\gamma_{\text{QF}} = 2.697 \times 10^7 a_0^{5/2}$, for vorticities $S = 0, 1, 3, 5$ under the action of the toroidal confining potential (7). All the configurations presented here are stationary solutions obtained by means of the ITP method. As N increases, both μ and energy increase monotonously for all multipole states, reflecting the increase of the repulsive-interaction energy. In contrast, the amplitude decreases due to the spreading of the respective wavefunctions. States with higher values of S exhibit larger energy and chemical potential for given N , and their amplitudes are consistently higher.

an even number of lobes, due to the phase-winding constraints. The origin of these multipole structures can be traced to the centrifugal force. For a vortex of charge S , the wave function $\psi = f(\rho, z)e^{iS\theta}$ generates a phase-gradient kinetic-energy term $S^2/(2\rho^2)$, which acts as an effective centrifugal potential, independent of density gradients, hence it is present even in the Thomas–Fermi regime. As S increases, the centrifugal pressure pushes the density outward and destabilizes the uniform annular profile. Typical stationary density profiles for different vorticity values are presented in Fig. 1. For $S = 0$, a ring-shaped structure appears, as shown in Fig. 1(a). When vorticity $S = 1$ is imparted, the centrifugal force causes the droplet to break the rotational symmetry and split in two distinct lobes, forming a dipole-like configuration, see Fig. 1(b). As the vorticity increases to $S = 2$, the VQD give rise to quadrupole-shaped modes, see Fig. 1(c). The growing centrifugal effect pushes the density outwards along the radial direction. By further increasing the vorticity to $S = 4, 5$ and 6 , higher-order multipole structures emerge, consisting of 8, 10 and 12 density lobes, respectively, as displayed in panels (d), (e), and (f) of Fig. 1. The lobes arrange themselves symmetrically around the radial axis, forming a necklace-like distribution as a result of the interplay of the phase winding, centrifugal expansion, and toroidal confinement. Figure 2 presents a magnified view of the density distribution in QDs composed of $N = 5000$ atoms in the absence of the LHY correction, $\gamma_{\text{QF}} = 0$. Although the obtained stationary profiles are similar to the LHY-stabilized states shown in Fig. 1, they are not self-bound droplets; instead, they constitute trap-bound stationary solutions maintained by the combined effect of the DDI anisotropy [86] and toroidal trapping potential. To clarify their energy character, the total energy is shown in Fig. 3 as a function of N for fixed vorticities S . The energy curves show that the ring-shaped state with $S = 0$ attains the lowest energy and therefore represents the ground state, while multipole configurations ($S = 1, 3, 5$) correspond to local extrema (metastable states). Thus, the LHY-free stationary pro-

files are regarded as ITP-generated solutions supported by the DDI anisotropy and the toroidal geometry, rather than as globally stable or long-lived droplets. We further emphasize that the energy metastability does not guarantee full dynamical stability. It is well known that dipolar droplets are not dynamically stable in the absence of the LHY term. The full stability analysis is therefore presented here only for the LHY-stabilized states, which are the main subject of the present work. Both Figs. 1 and 2 demonstrates that the number n of the density lobes (poles of the multipole patterns) increases with the increase of vorticity S . For $S \leq 6$, the trend approximately follows an empirical relation, $n = 2S$. However, this correspondence is not a universal rule and tends to deviate for higher vorticities, where the interplay between the centrifugal expansion, nonlinear interactions, and confinement geometry leads to more complex droplet distributions. Figure 4 represents contour plots of the 2D density profiles in the (x, y) plane for the multipole QDs of the same types as displayed in Fig. 1. The panels correspond to: (a) $S = 0$, (b) $S = 1$, (c) $S = 2$, (d) $S = 4$, (e) $S = 5$, and (f) $S = 6$, with the atom number fixed at $N = 2000$. The insets display the corresponding phase profiles for each configuration, highlighting the phase winding and the topological structure of the droplets. The phase profiles of these multipole lobes exhibit out-of-phase behavior along the z -direction. The lobes feature alternating phase patterns, which results in effective repulsive interactions. It should be noted that the configurations presented in Figs. (1-4) are stationary solutions obtained by means of the ITP method. Their existence does not automatically imply dynamical stability, which is tested below using the perturbed real-time propagation. Proceeding to characteristics of families of the QD modes, Fig. 5(a) presents the chemical potential μ as a function of the atom number N for distinct vorticities considered. For all the vorticities considered, μ exhibits a positively slope the $\mu(N)$ dependence, which is consistent with the anti-Vakhitov-Kolokolov (anti-VK) stability criterion, $d\mu/dN > 0$ [87]. The usual VK cri-

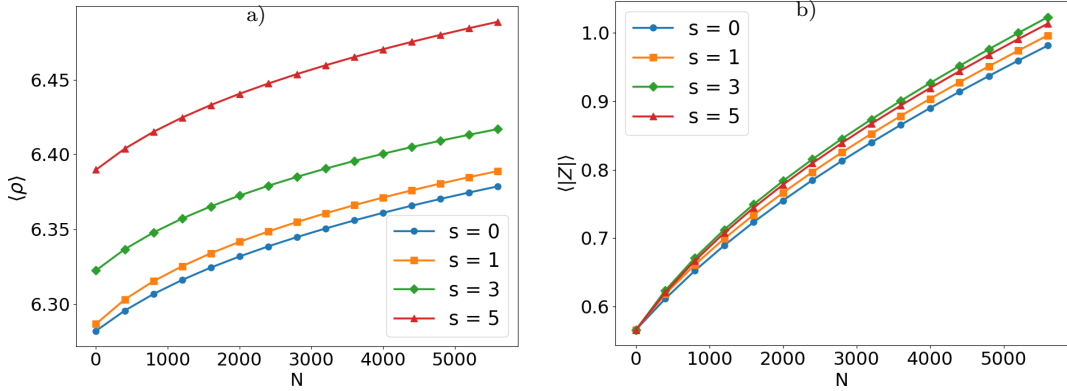


FIG. 6. (a) Radial extension $\langle \rho \rangle$ and (b) axial thickness $\langle |z| \rangle$ as functions of atom number N , for different vorticities $S = 0, 1, 3, 5$, as calculated for the DDI length $a_{\text{dd}} = 130.8a_0$, scattering length $a = 100a_0$, and $\gamma_{\text{QF}} = 2.697 \times 10^7 a_0^{5/2}$. All the configurations are stationary solutions obtained by means of the ITP method. The radial size increases significantly with the growth of N and S due to the centrifugal expansion of the rotating states. In contrast, the axial thickness grows slower and shows less sensitivity to the vorticity, reflecting the stronger confinement in the axial direction.

terion, $d\mu/dN < 0$, is the necessary stability condition in systems dominated by the self-attractive nonlinearity [88, 89]. It is seen that the inclusion of the LHY correction universally stabilizes the system, while increasing its chemical potential and energy. Further, Fig. 5(b) displays the total energy as a function of N . As expected for the condensate with the repulsive interaction, the energy increases with the growth of the atom number. The increase rate is higher for multipolar QDs states due to their additional gradient energy.

Figure 5(c) shows the amplitude as a function of the atom number N for various vorticities. In contrast to the trends observed for the chemical potential and energy, the amplitude decreases with the increase of N for all vorticities. This behavior results from the enhanced centrifugal effect associated with higher vorticity, which causes the condensate to expand radially, thereby lowering the amplitude. To understand the 3D structure of QDs under the action of the toroidal confinement, we computed the average radial extension $\langle \rho \rangle$ and axial thickness $\langle |z| \rangle$, as per Eq. (13), as functions of the total atom number N for distinct vorticity values S ,

$$\langle \rho \rangle = \iiint \sqrt{x^2 + y^2} |\psi(x, y, z)|^2 dx dy dz, \quad (13a)$$

$$\langle |z| \rangle = \iiint |z| |\psi(x, y, z)|^2 dx dy dz, \quad (13b)$$

with the results displayed in Fig. 6. As shown in Fig. 6(a), the radial size $\langle \rho \rangle$ increases with the growth of both N and vorticity S . This is attributed to the centrifugal effect associated with the vorticity, which leads to an outward pressure in the radial direction, thereby stretching the QD radially. Note that, as shown in Fig. 6(a), the radial thickness $\langle \rho \rangle$ increases with S , whereas the peak density $|\psi|_{\text{max}}^2$ exhibits a decreasing trend. This behavior is a natural consequence of the centrifugal effect introduced by the phase winding in the multipole states. Indeed, as S increases, the system experiences

enhanced radial spreading due to the rotational kinetic-energy pressure, reducing the local density in the core. This argument highlights the compressible 3D structure of the multipole QDs, which adjust their shape and density distribution under the action of the toroidal confinement. The axial thickness $\langle |z| \rangle$, plotted in Fig. 6(b), also increases with N , but exhibits relatively weak variation across different vorticity values. These features suggest that the axial confinement, being tighter, resists the expansion caused by the enhanced centrifugal force. Fig. 7 shows the variation of the chemical potential μ in panel (a), and energy E in (b) with respect to S for different atom numbers ($N = 1000, 2000, 3000, 5000$). In Fig. 7(b), it is observed that the ground state (energy minimum) corresponds to $S = 0$ for each atom number N . The energy of the other configurations increases with S up to $S = 10$, while for $S = 11$ and $S = 12$ both the chemical potential and energy decreases. For a large value of S , the centrifugal term $S^2/(2\rho^2)$ forces the density annulus to expand outward. Therefore, the droplet makes both the peak density and LHY contribution lower, leading to the decrease of μ and E for $S = 11, 12$.

III.2. Dynamical states of multipole droplets under the action of the toroidal confinement

The above-mentioned anti-VK criterion, $d\mu/dN > 0$, observed in Fig. 5(a), is a necessary but not sufficient stability condition. To assess the full stability of the QDs configurations, we performed the real-time simulations by perturbing the stationary solutions by 1% random noise and monitoring the subsequent evolution. In this way, we explicitly distinguish between the stationary states (Figs. 1-4) and dynamical stability under the action of perturbations. Characteristic examples of the perturbed dynamics are presented in Fig. 8. It is observed that the QDs corresponding to $S = 0$ remain sta-

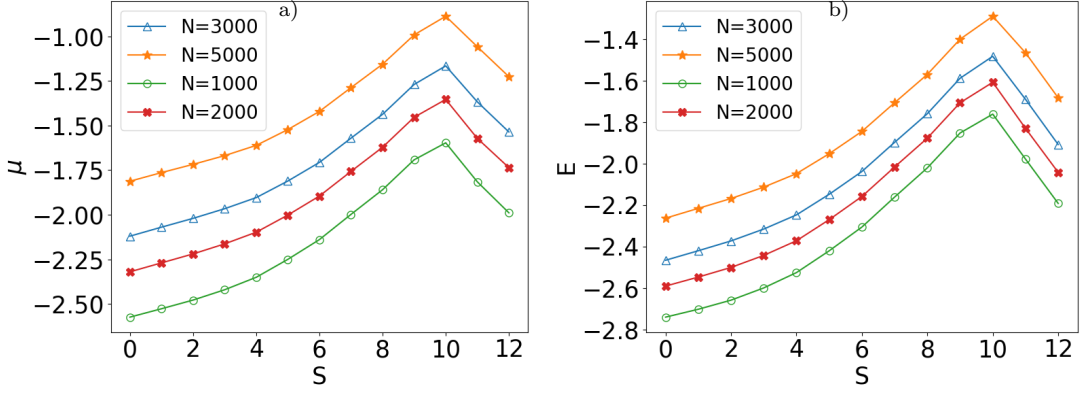


FIG. 7. The variation of (a) the chemical potential μ and (b) total energy E vs. vorticity S , as produced by the stationary solutions for different numbers of atoms with DDI length $a_{\text{dd}} = 130.8a_0$, scattering length $a = 100a_0$, and $\gamma_{\text{QF}} = 2.697 \times 10^7 a_0^{5/2}$. The ground-state configuration corresponds to $S = 0$, with both the energy E and chemical potential μ increasing gradually till $S = 10$, followed by the decrease of E and μ for $S = 11$ and 12 .

ble, as shown in Fig. 8(a), at time $t = 4t_0 \approx 10.44$ ms, with $t_0 = 2.61$ ms. In contrast, the multipolar QDs with $S = 1, 2, 5, 6, 7, 8$ and 10 (Figs. 8(b–h)) exhibit clear signatures of instability, with the instability growth rate increasing with S . The instability times reported here are typically in the range of 1 – 10 ms, which is short but still within experimentally relevant timescales [60]. Although they are unstable, QDs persist under small perturbations with the random noise applied at the level of 0.1% during the time interval $t = 0.4t_0 \approx 1.044$ ms, as shown in Fig. 9(a) and (b) for the configurations $S = 1$ and $S = 6$. This behavior reflects a transient robustness rather than metastability. In contrast, the configurations with $S = 7$ and $S = 8$ undergo fragmentation, as shown in Figs. 9c–d). Figures 10(a) and (b) further explore the role of the LHY correction in the high-vorticity regime at $t = 4.0t_0 \approx 10.44$ ms. For $S = 12$, the enhanced centrifugal effect drives neighboring density lobes to approach each other. When the LHY correction is included, its additional repulsive contribution counteracts this tendency, preventing full coalescence and resulting in a partially merged unstable configuration, as seen in Fig. 10(a). In contrast, when $\gamma_{\text{QF}} = 0$ (no LHY term), the system enters the attraction regime that favors the full merger of the lobes, leading to the formation of a ring-like configuration, displayed in Fig. 10(b).

To further examine the dynamical behavior of the QDs, we display the perturbed evolution of their radial $\langle \rho \rangle$ and axial $\langle |z| \rangle$ widths, as obtained from real-time simulations. To this end, the stationary modes, produced by means of the ITP method, were perturbed by a 1% random noise and then used as initial conditions for the real-time propagation, with vorticities $S = 0, 1, 3$ and $N = 5000$ atoms. Figures 11(a) and (b) show the evolution of $\langle \rho \rangle$ and $\langle |z| \rangle$, respectively, for trap parameters $d = \sqrt{6}$ and $z_0 = \sqrt{6}$. In the case of $S = 0$, corresponding to the energetically stable ground state, the QD remains robust against the applied perturbation, with the radial width remaining nearly constant and weak oscillations appearing in the

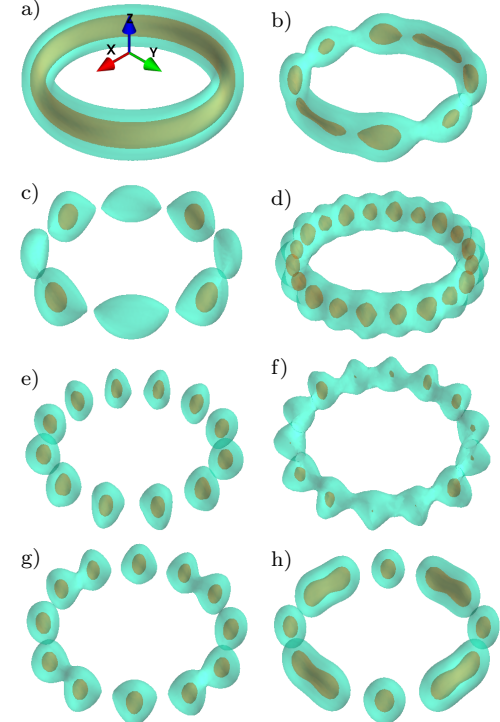


FIG. 8. The real-time dynamics of QDs perturbed random noise at the 1% level for various vorticities at time $t = 4.0t_0 \approx 10.44$ ms, with $t_0 = 2.61$ ms. (a) $S = 0$, (b) $S = 1$, (c) $S = 2$, (d) $S = 5$, (e) $S = 6$, (f) $S = 7$, (g) $S = 8$, and (h) $S = 10$, highlighting the transition from the stable to unstable behavior under strong perturbations (1% noise) as S increases. Under the action of this perturbation, only the state with $S = 0$ remains stable (black circle in Fig. 12). Higher-vorticity states, with $S \geq 1$, exhibit unstable behavior; however, some of these states persist under the action of weaker perturbations for short time intervals. All the results are produced for $N = 5000$, $a_{\text{dd}} = 130.8a_0$, scattering length $a = 100a_0$, and the LHY coefficient $\gamma_{\text{QF}} = 2.697 \times 10^7 a_0^{5/2}$.

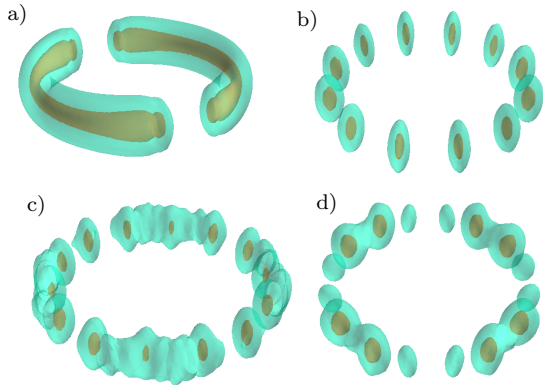


FIG. 9. The real-time dynamics of QDs perturbed by random noise at the 0.1% level, for different vorticities. Panels (a)-(d) display the perturbed evolution of the QDs for $N = 5000$ with the DDI length $a_{dd} = 130.8a_0$, scattering length $a = 100a_0$, and the LHY coefficient $\gamma_{QF} = 2.697 \times 10^7 a_0^{5/2}$ at time $t = 0.4t_0 \approx 1.044$ ms, with $t_0 = 2.61$ ms. (a) $S = 1$, (b) $S = 6$, (c) $S = 7$, (d) $S = 8$. The $S = 1$ and $S = 6$ configurations retain their structure for short times under weak perturbations, exhibiting only a transient robustness (represented by blue stars in Fig. 12), while the modes with $S = 7$ and $S = 8$ are unstable (represented by red triangles in Fig. 12), decaying even under the action of the weak noise with the 0.1% strength.

axial direction. In contrast, the vortical configurations with $S = 1$ and $S = 3$ exhibit pronounced oscillatory dynamics in both the radial and axial widths, reflecting the excitation of collective modes by the initial perturbation. For the wider trap with $d = \sqrt{8}$ and $z_0 = \sqrt{8}$, used in Figs. 11(c,d), the oscillation frequency remains essentially unchanged for all vorticities. However, the oscillation amplitude increases noticeably for the vortical states $S = 1$ and $S = 3$, as may be expected from trap-induced collective modes. These observations suggest that the oscillatory dynamics is determined by the external confinement.

Finally, in Fig. 12 we map stability boundaries of QDs with different vorticities S , as revealed by systematic real-time simulations of the perturbed evolution. The $S = 0$ configuration (black circles) always corresponds to the dynamically stable ground state, preserving its shape over the longest simulated evolution time, $t \approx 10.44$ ms. The configurations with $1 \leq S \leq 6$ (blue stars) remain intact over relatively short evolution times, up to $t \approx 1.044$ ms, reflecting a transient robustness under the action of weak, 0.1%, random perturbations. In contrast, states with $S \geq 7$ (up to the largest value considered here, $S = 12$, which are denoted by red triangles) are clearly unstable and rapidly decay, even under the action of the weak perturbation (0.1%), during the same short time $t \approx 1.044$ ms. The configurations labeled $8a, 9a - 9d, 10a$ along the horizontal line corresponding to $N = 5000$ are cross-referenced with the real-time simulations displayed in Figs. 8-10.

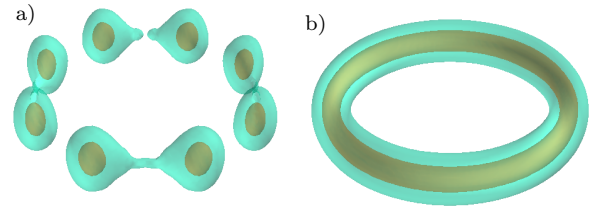


FIG. 10. The role of the LHY correction is illustrated by the real-time dynamics of QDs with vorticity $S = 12$ and atom number $N = 5000$, DDI length $a_{dd} = 130.8a_0$, and scattering length $a = 100a_0$, evaluated at $t = 4.0t_0 \approx 10.44$ ms with $t_0 = 2.61$ ms. Panel (a) includes the LHY correction term with $\gamma_{QF} = 2.697 \times 10^7 a_0^{5/2}$. Due to enhanced centrifugal effect, the poles begin to merge with the neighboring poles, while the repulsive LHY term prevents the complete merging, resulting in an unstable configuration (represented by a red triangle in Fig. 12). Panel (b) corresponds to the case without the correction, $\gamma_{QF} = 0$, resulting in an attractive regime leading to complete merger of the droplets into a ring-shaped configuration. All results are obtained in the absence of external perturbations.

III.3. Stationary states of multipole droplets under Gaussian Confinement

Finally, we investigated the effect of the external confinement, replacing the ring-shaped (toroidal) trap (7) by the Gaussian potential, with $\rho_0 = 0$, to analyze the formation and structure of the VQDs under different geometric constraints. Figure (13) illustrates the formation of multipole QDs under the action of the Gaussian potential. Panels (a) - (f) represent 2D density distribution of the stable QD for $S = 1 - 6$ configurations, respectively. It is observed for higher vorticity values ($S = 4, 5, 6$), the density distribution exhibits distinct high-density lobes alternating with low-density regions, reflecting the underlying angular modulation induced by the higher-order vorticity. The angular modulation arises due to the inability of the Gaussian trap to directly accommodate high-vorticity states. Unlike the toroidal trap, which naturally supports the circulating superflow and allows the density to spread uniformly along the ring, the centrally peaked Gaussian trapping potential keeps the condensate near the origin. Therefore, the central confinement and centrifugal effects lead to the breaking of the axial symmetry and results in petal-shaped multipole structures. This comparison demonstrates that multipole droplets also arise from a geometry-dependent balance between the centrifugal effect, the trapping potential, and the nonlinear interactions. Thus, the findings of this section reinforce the central result that trapping geometry plays a critical role in determining the morphology VQDs, complementing the analysis presented in Sec. III.1 and Sec. III.2.

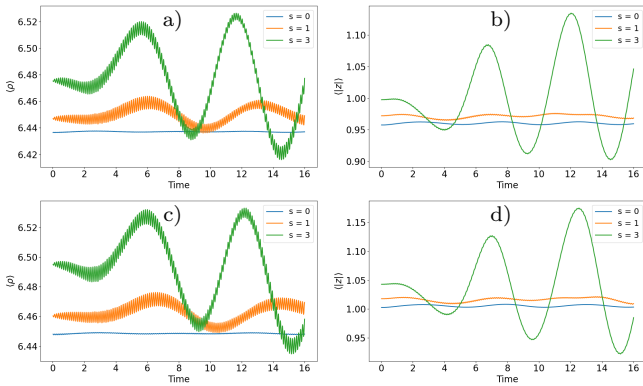


FIG. 11. Real-time evolution of the radial $\langle \rho \rangle$ (a,c) and axial $\langle |z| \rangle$ (b,d) widths of QDs with vorticities $S = 0, 1$, and 3 , $N = 5000$ atoms, DDI length $a_{dd} = 130.8a_0$, scattering length $a = 100a_0$, and $\gamma_{QF} = 2.697 \times 10^7 a_0^{5/2}$, for different trap widths. Panels (a,b) correspond to the trap parameters $d = \sqrt{6}$ and $z_0 = \sqrt{6}$ with $p = 6$ and $\rho_0 = 2\pi$, while panels (c,d) correspond to a wider trap with $d = \sqrt{8}$ and $z_0 = \sqrt{8}$ and the same values $p = 6$ and $\rho_0 = 2\pi$. The stationary state, produced by means of ITP for each vorticity, is used as the initial condition for real-time evolution, which is perturbed by a 1% random noise. For panels (a,b), the $S = 0$ droplet remains stable, exhibiting an almost constant radial width and weak axial oscillations, whereas the vortical configurations with $S = 1$ and $S = 3$ display growing oscillatory dynamics in both radial and axial directions. For the wider trap in panels (c,d), the oscillation frequency remains unchanged, while the oscillation amplitude increases for all the states, indicating enhanced excitation of the trap-induced collective modes.

IV. CONCLUSION

We have investigated the emergence, structure, and stability of the 3D ring-shaped and multipole QDs (quantum droplets) in the dipolar BEC confined by the toroidal potential. The interplay of the DDI (dipole-dipole interactions) with the beyond-mean-field LHY (Lee-Huang-Yang) correction, produces a broad variety of the vorticity-carrying 3D QD necklace-like arrays. Our results demonstrate that the toroidal geometry naturally facilitates the formation of VQDs (vortex QDs), which exhibit donut-shaped density distributions with the internal phase-imprinted vorticity. With increasing vorticity S , the VQD configurations evolve into multipole patterns, with the number of density peaks (poles) approximately given by $n = 2S$, up to $S \leq 6$. The multipolar structures are stabilized by the combined action of the confinement geometry, nonlocal DDI, and the effect of quantum fluctuations represented by the LHY term. Remarkably, even in the absence of the latter one, the QD remains robustly self-bound, as the DDI alone can support stable states in the combination with the trapping potential, preventing the onset of the collapse. Increasing the atom number N , naturally leads to an expansion of the droplet along the azimuthal direction. Through systematic numerical simulations, we have investigated

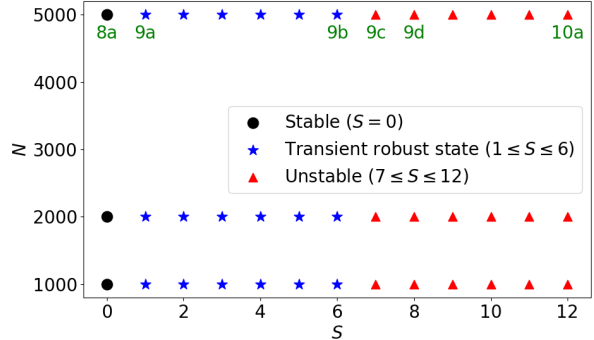


FIG. 12. Stability boundaries of the QD ring-shaped configurations, as inferred from the systematic simulations of the perturbed evolution, for different values of the atom number N and vorticity S . Black circles represent stable ground-state configurations obtained for $S = 0$, which preserve their structure up to $t = 4.0 t_0 \approx 10.44$ ms under the action of the 1% random perturbation. States with $1 \leq S \leq 6$, indicated by blue stars, are short-lived (transiently stable) ones, retaining their structure only up to $t = 0.4 t_0 \approx 1.044$ ms, under the action of a weaker 0.1% perturbation. Configurations with $S \geq 7$ (up to the largest value considered here, $S = 12$), denoted by red triangles, are unstable, decaying under the action of the weak 0.1% perturbation during the time $t \approx 1.044$ ms. The markers placed at the horizontal line corresponding to the atom number $N = 5000$ refer to the simulation results presented above: the point labeled $8a$ (the black circle) corresponds to Fig. 8(a), the points labeled $9a$ – $9d$ (blue stars) correspond to Figs. 9(a–d), and the point labeled $10a$ (the red triangle) corresponds to Fig. 10(a). The other parameters are $a_{dd} = 130.8a_0$, $a = 100a_0$, and $\gamma_{QF} = 2.697 \times 10^7 a_0^{5/2}$.

the effects of varying N and vorticity S on the chemical potential, energy, amplitude, and radial and axial widths of the QDs. They satisfy the anti-VK necessary stability condition, where the full stability has been verified by means of systematic simulations of the perturbed evolution. The total energy of the QD stationary states gradually increases as a function of N , higher-vorticity states exhibiting larger energies due to the centrifugal effect, which also leads to the reduction in the peak density as the radial expansion of the QD structure. The radial width consistently increases with N for all values of the vorticity, as expected. In contrast, the axial (z) width shows only minor variations, indicating an essentially tighter confinement in that direction.

The stability analysis based in the direct simulations demonstrates that, while the ground-state QDs with $S = 0$ exhibit complete stability, multipole VQDs became increasingly susceptible to structural deformations and, eventually, fragmentation with the increase of vorticity S . The results are summarized as follows: the configurations with $1 \leq S \leq 6$ survive under the action of mild random perturbations, with the relative amplitude $\sim 0.1\%$, whereas a stronger perturbation with the amplitude $\sim 1\%$ leads to fragmentation, indicating the transient robustness. In contrast, the ones with

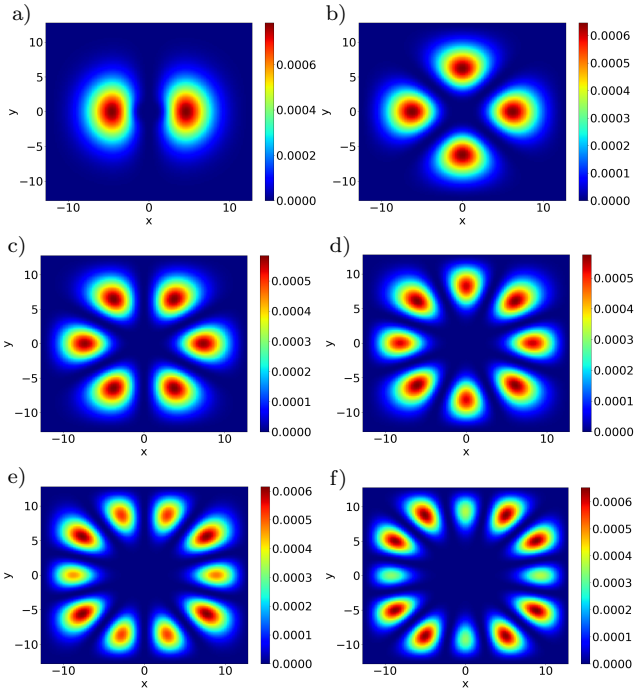


FIG. 13. Contour plots of the 2D density projection of stable multipole QDs in the (x, y) plane, under the action of the Gaussian confinement represented by potential (7) with $\rho_0 = 0$, $p = -10$, $d = z_0 = 1$. Panels (a) - (f) pertain to vorticities $S = 1 - 6$, respectively. An increase in the vorticity results in structural variations of the QDs. All the results are obtained for the atom number $N = 2000$, DDI length $a_{\text{dd}} = 130.8a_0$, scattering length $a = 100a_0$, and the strength of the LHY correction $\gamma_{\text{QF}} = 2.697 \times 10^7 a_0^{5/2}$.

$S \geq 7$ are definitely unstable. We have also highlighted the significant role of the trapping geometry, by comparing the properties of the QDs in the toroidal and Gaussian confinements. The toroidal potential supports persistent superflow, allowing the stable higher-order states. However, when the trap is replaced by the centrally peaked Gaussian, the condensate undergoes symmetry breaking, resulting in angular fragmentation even at moderate vorticities. This outcome originates from the interplay of the azimuthal dynamics and trapping geometry, with the competition of the centrifugal expansion and the central localization leading to the spontaneous pattern formation. In summary, this work presents a comprehensive analysis of the 3D ring-shaped and multipole QDs in the dipolar BEC under the combined action of the toroidal trap and LHY correction. These findings advance the theoretical understanding of structured states of the quantum matter and offer insights in the possibility of the experimental realization of novel VQD states in ultracold gases of magnetic atoms, such as ^{164}Dy . Future directions of the studies may be aimed at the role of spin-orbit coupling and overall rotation, potentially uncovering new regimes of supersolidity, topological excitations, and quantum turbulence in dipolar condensates.

Acknowledgment: S. Sanjay and S. Saravana Veni acknowledge Amrita Vishwa Vidyapeetham, Coimbatore, where this work was supported under Amrita Seed Grant (File Number: ASG2022141).

[1] A. Bulgac, Dilute quantum droplets, *Phys. Rev. Lett.* **89**, 050402 (2002).

[2] Z.-H. Luo, W. Pang, B. Liu, Y.-Y. Li, and B. A. Malomed, A new form of liquid matter: Quantum droplets, *Front. Phys.* **16**, 1–21 (2021).

[3] M. Guo and T. Pfau, A new state of matter of quantum droplets, *Front. Phys.* **16**, 32202 (2021).

[4] M. Boninsegni and N. V. Prokof'ev, Colloquium: Supersolids: What and where are they?, *Rev. Mod. Phys.* **84**, 759–776 (2012).

[5] A. Recati and S. Stringari, Supersolidity in ultracold dipolar gases, *Nat. Rev. Phys.* **5**, 735–743 (2023).

[6] P. Ilzhöfer, M. Sohmen, G. Durastante, C. Politi, A. Trautmann, G. Natale, G. Morpurgo, T. Giamarchi, L. Chomaz, M. J. Mark, and F. Ferlaino, Phase coherence in out-of-equilibrium supersolid states of ultracold dipolar atoms, *Nat. Phys.* **17**, 356 (2021).

[7] N. Verhelst and J. Tempere, Vortex structures in ultracold atomic gases, in *Vortex Dynamics and Optical Vortices*, edited by H. Perez-de-Tejada (IntechOpen, Rijeka, 2017) Chap. 1.

[8] L. Klaus, T. Bland, E. Poli, C. Politi, G. Lamporesi, E. Casotti, R. N. Bisset, M. J. Mark, and F. Ferlaino, Observation of vortices and vortex stripes in a dipolar condensate, *Nat. Phys.* **18**, 1453 (2022).

[9] A. Chaika, A. Richaud, and A. Yakimenko, Making ghost vortices visible in two-component Bose–Einstein condensates, *Phys. Rev. Res.* **5**, 023109 (2023).

[10] D. S. Petrov, Quantum mechanical stabilization of a collapsing Bose–Bose mixture, *Phys. Rev. Lett.* **115**, 155302 (2015).

[11] D. S. Petrov and G. E. Astrakharchik, Ultradilute low-dimensional liquids, *Phys. Rev. Lett.* **117**, 100401 (2016).

[12] T. W. Neely, E. C. Samson, A. S. Bradley, M. J. Davis, and B. P. Anderson, Observation of vortex dipoles in an oblate Bose–Einstein condensate, *Phys. Rev. Lett.* **104**, 160401 (2010).

[13] C. N. Weiler, T. W. Neely, D. R. Scherer, A. S. Bradley, M. J. Davis, and B. P. Anderson, Spontaneous vortices in the formation of Bose–Einstein condensates, *Nature* **455**, 948 (2008).

[14] A. Macia, J. Sánchez-Baena, J. Boronat, and F. Mazzanti, Droplets of trapped quantum dipolar bosons, *Phys. Rev. Lett.* **117**, 205301 (2016).

[15] F. Cinti, A. Cappellaro, L. Salasnich, and T. Macrì, Superfluid filaments of dipolar bosons in free space, *Phys. Rev. Lett.* **119**, 215302 (2017).

[16] V. Ciković, K. Dželalija, P. Stipanović, L. Vranješ Markić, and J. Boronat, Ultradilute quantum liquid drops, *Phys. Rev. B* **97**, 140502(R) (2018).

[17] L. Parisi, G. E. Astrakharchik, and S. Giorgini, Liquid state of one-dimensional Bose mixtures: A quantum Monte Carlo study, *Phys. Rev. Lett.* **122**, 105302 (2019).

[18] V. Cikojević, L. Vranješ Markić, G. E. Astrakharchik, and J. Boronat, Universality in ultradilute liquid Bose-Bose mixtures, *Phys. Rev. A* **99**, 023618 (2019).

[19] V. Cikojević, L. Vranješ Markić, and J. Boronat, Finite-range effects in ultradilute quantum drops, *New J. Phys.* **22**, 053045 (2020).

[20] I. Ferrier-Barbut, H. Kadau, M. Schmitt, M. Wenzel, and T. Pfau, Observation of quantum droplets in a strongly dipolar Bose gas, *Phys. Rev. Lett.* **116**, 215301 (2016).

[21] F. Böttcher, J.-N. Schmidt, J. Hertkorn, K. S. H. Ng, S. D. Graham, M. Guo, T. Langen, and T. Pfau, New states of matter with fine-tuned interactions: quantum droplets and dipolar supersolids, *Rep. Prog. Phys.* **84**, 012403 (2020).

[22] P. Cheiney, C. R. Cabrera, J. Sanz, B. Naylor, L. Tanzi, and L. Tarruell, Bright soliton to quantum droplet transition in a mixture of Bose-Einstein condensates, *Phys. Rev. Lett.* **120**, 135301 (2018).

[23] G. Semeghini, G. Ferioli, L. Masi, C. Mazzinghi, L. Wolswijk, F. Minardi, M. Modugno, G. Modugno, M. Inguscio, and M. Fattori, Self-bound quantum droplets of atomic mixtures in free space, *Phys. Rev. Lett.* **120**, 235301 (2018).

[24] C. D'Errico, A. Burchianti, M. Prevedelli, L. Salasnich, F. Ancilotto, M. Modugno, F. Minardi, and C. Fort, Observation of quantum droplets in a heteronuclear bosonic mixture, *Phys. Rev. Res.* **1**, 033155 (2019).

[25] A. Burchianti, C. D'Errico, M. Prevedelli, L. Salasnich, F. Ancilotto, M. Modugno, F. Minardi, and C. Fort, A dual-species Bose-Einstein condensate with attractive interspecies interactions, *Condens. Matter* **5**, 21 (2020).

[26] C. D'Errico, M. Zaccanti, M. Fattori, G. Roati, M. Inguscio, G. Modugno, and A. Simoni, Feshbach resonances in ultracold ^{39}K , *New J. Phys.* **9**, 223 (2007).

[27] G. C. Katsimiga, S. I. Mistakidis, B. A. Malomed, D. J. Frantzeskakis, R. Carretero-Gonzalez, and P. G. Kevrekidis, Interactions and dynamics of one-dimensional droplets, bubbles and kinks, *Condens. Matter* **8**, 67 (2023).

[28] Y. Hu, Y. Fei, X.-L. Chen, and Y. Zhang, Collisional dynamics of symmetric two-dimensional quantum droplets, *Front. Phys.* **17**, 61505 (2022).

[29] G. Ferioli, G. Semeghini, L. Masi, G. Giusti, G. Modugno, M. Inguscio, A. Gallemí, A. Recati, and M. Fattori, Collisions of self-bound quantum droplets, *Phys. Rev. Lett.* **122**, 090401 (2019).

[30] A. Debnath, A. Khan, and B. A. Malomed, Interaction of one-dimensional quantum droplets with potential wells and barriers, *Commun. Nonlinear Sci. Numer. Simul.* **126**, 107457 (2023).

[31] M. Schmitt, M. Wenzel, F. Böttcher, I. Ferrier-Barbut, and T. Pfau, Self-bound droplets of a dilute magnetic quantum liquid, *Nature* **539**, 259 (2016).

[32] I. Ferrier-Barbut, H. Kadau, M. Schmitt, M. Wenzel, and T. Pfau, Observation of quantum droplets in a strongly dipolar Bose gas, *Phys. Rev. Lett.* **116**, 215301 (2016).

[33] F. Wächtler and L. Santos, Ground-state properties and elementary excitations of quantum droplets in dipolar Bose-Einstein condensates, *Phys. Rev. A* **94**, 043618 (2016).

[34] K.-T. Xi and H. Saito, Droplet formation in a Bose-Einstein condensate with strong dipole-dipole interaction, *Phys. Rev. A* **93**, 011604 (2016).

[35] F. Böttcher, M. Wenzel, J.-N. Schmidt, M. Guo, T. Langen, I. Ferrier-Barbut, T. Pfau, R. Bombín, J. Sánchez-Baena, J. Boronat, and F. Mazzanti, Dilute dipolar quantum droplets beyond the extended Gross-Pitaevskii equation, *Phys. Rev. Res.* **1**, 033088 (2019).

[36] L. E. Young-S and S. K. Adhikari, Supersolid-like square- and honeycomb-lattice crystallization of droplets in a dipolar condensate, *Phys. Rev. A* **105**, 033311 (2022).

[37] L. E. Young-S and S. K. Adhikari, Supersolid-like square- and triangular-lattice crystallization of dipolar droplets in a box trap, *Eur. Phys. J. Plus* **137**, 1153 (2022).

[38] L. E. Young-S and S. K. Adhikari, Mini droplet, mega droplet and stripe formation in a dipolar condensate, *Physica D* **455**, 133910 (2023).

[39] R. Hołyst, M. Litniewski, D. Jakubczyk, K. Kolwas, M. Kolwas, K. Kowalski, S. Migacz, S. Palesa, and M. Zientara, Evaporation of freely suspended single droplets: experimental, theoretical and computational simulations, *Rep. Prog. Phys.* **76**, 034601 (2013).

[40] K. E. Wilson, N. Westerberg, M. Valiente, C. W. Duncan, E. M. Wright, P. Öhberg, and D. Faccio, Observation of photon droplets and their dynamics, *Phys. Rev. Lett.* **121**, 133903 (2018).

[41] S. Sanjay, S. Saravana Veni, and Boris A. Malomed, Vortex droplets and lattice patterns in two-dimensional traps: A photonic spin-orbit-coupling perspective, *Chaos, Solitons & Fractals*, **197**, 116441 (2025).

[42] S. Deekshita, S. Sanjay, S. Saravana Veni, C.B. Tabi, and T.C. Kofané, Synergistic effects of spin-orbit coupling and intercomponent interactions in two-component (2+1)D photonic fields, *Chaos, Solitons & Fractals*, **199**, 116806 (2025).

[43] D. Mihalache, Localized structures in optical and matter-wave media: A selection of recent studies, *Rom. Rep. Phys.* **73**, 403 (2021).

[44] B. A. Malomed, *Multidimensional Solitons* (AIP Publishing, Melville, NY, 2022.)

[45] D. Mihalache, Localized structures in optical media and Bose-Einstein condensates: An overview of recent theoretical and experimental results, *Rom. Rep. Phys.* **76**, 402 (2024).

[46] D. Mihalache, D. Mazilu, L.-C. Crasovan, I. Towers, A. V. Buryak, B. A. Malomed, L. Torner, J. P. Torres, and F. Lederer, Stable spinning optical solitons in three dimensions, *Phys. Rev. Lett.* **88**, 073902 (2002).

[47] A. S. Reyna and C. B. de Araújo, High-order optical nonlinearities in plasmonic nanocomposites – a review, *Adv. Opt. Photonics.* **9**, 720 (2017).

[48] Y. Li, Z. Chen, Z. Luo, C. Huang, H. Tan, W. Pang, and B. A. Malomed, Two-dimensional vortex quantum droplets, *Phys. Rev. A* **98**, 063602 (2018).

[49] L. Dong, K. Shi, and C. Huang, Internal modes of two-dimensional quantum droplets, *Phys. Rev. A* **106**, 053303 (2022).

[50] L. Dong, D. Liu, Z. Du, K. Shi, and W. Qi, Bistable multipole quantum droplets in binary Bose-Einstein condensates, *Phys. Rev. A* **105**, 033321 (2022).

[51] Y. V. Kartashov, B. A. Malomed, L. Tarruell, and L. Torner, Three-dimensional droplets of swirling superfluids, *Phys. Rev. A* **98**, 013612 (2018).

[52] G. Li, Z. Zhao, B. Liu, Y. Li, Y. V. Kartashov, and B. A. Malomed, Can vortex quantum droplets be realized experimentally?, *Front. Phys.* **20**, 013401 (2025).

[53] Y. V. Kartashov, B. A. Malomed, and L. Torner,

Metastability of quantum droplet clusters, *Phys. Rev. Lett.* **122**, 193902 (2019).

[54] M. N. Tengstrand, P. Stürmer, E. Ö. Karabulut, and S. M. Reimann, Rotating binary Bose-Einstein condensates and vortex clusters in quantum droplets, *Phys. Rev. Lett.* **123**, 160405 (2019).

[55] L. Dong, M. Fan, and B. A. Malomed, Three-dimensional vortex and multipole quantum droplets in a toroidal potential, *Chaos, Solitons & Fractals* **188**, 115499 (2024).

[56] J. Polo, W. J. Chetcuti, T. Haug, A. Minguzzi, K. Wright, and L. Amico, Persistent currents in ultracold gases, *Phys. Rep.* **1137**, 1-70 (2025)

[57] L. Dong, M. Fan, and B. A. Malomed, Stable higher-charge vortex solitons in the cubic-quintic medium with a ring potential, *Opt. Lett.* **48**, 4817 (2023).

[58] L. Dong, M. Fan, and B. A. Malomed, Stable higher-order vortex quantum droplets in an annular potential, *Chaos, Solitons & Fractals* **179**, 114472 (2024).

[59] L. Dong, M. Fan, C. Huang, and B. A. Malomed, Multipole solitons in competing nonlinear media with an annular potential, *Phys. Rev. A* **108**, 063501 (2023).

[60] A. Cidrim, F. E. A. dos Santos, E. A. L. Henn, and T. Macrì, Vortices in self-bound dipolar droplets, *Phys. Rev. A* **98**, 023618 (2018).

[61] G. Li, X. Jiang, B. Liu, Z. Chen, B. A. Malomed, and Y. Li, Two-dimensional anisotropic vortex quantum droplets in dipolar Bose-Einstein condensates, *Front. Phys.* **19**, 22202 (2024).

[62] N. Murray, M. Krygier, M. Edwards, K. C. Wright, G. K. Campbell, and C. W. Clark, Probing the circulation of ring-shaped Bose-Einstein condensates, *Phys. Rev. A* **88**, 053615 (2013).

[63] K. C. Wright, R. B. Blakestad, C. J. Lobb, W. D. Phillips, and G. K. Campbell, Threshold for creating excitations in a stirred superfluid ring, *Phys. Rev. A* **88**, 063633 (2013).

[64] A. Muñoz Mateo, A. Galleí, M. Guilleumas, and R. Mayol, Persistent currents supported by solitary waves in toroidal Bose-Einstein condensates, *Phys. Rev. A* **91**, 063625 (2015).

[65] M. Nilsson Tengstrand, D. Boholm, R. Sachdeva, J. Bengtsson, and S. M. Reimann, Persistent currents in toroidal dipolar supersolids, *Phys. Rev. A* **103**, 013313 (2021).

[66] A. Bhardwaj, I. Agullo, D. Kranas, J. H. Wilson, and D. E. Sheehy, Entanglement in an expanding toroidal Bose-Einstein condensate, *Phys. Rev. A* **109**, 013305 (2024).

[67] N. Bazhan, A. Svetlichnyi, D. Pfeiffer, D. Derr, G. Birk, and A. Yakimenko, Generation of Josephson vortices in stacked toroidal Bose-Einstein condensates, *Phys. Rev. A* **106**, 043305 (2022).

[68] L. E. Young-S and S. K. Adhikari, Dipole-mode and scissors-mode oscillations of a dipolar supersolid, *Phys. Rev. A* **107**, 053318 (2023).

[69] S. K. Adhikari, Quasi-one- and quasi-two-dimensional symbiotic solitons bound by dipolar interaction, *Phys. Rev. E* **109**, 064206 (2024).

[70] L. E. Young-S., P. Muruganandam, A. Balaž, and S. K. Adhikari, OpenMP Fortran programs for solving the time-dependent dipolar Gross-Pitaevskii equation, *Comput. Phys. Commun.* **286**, 108669 (2023).

[71] S. K. Adhikari, Spatially periodic states in a strongly dipolar ^{164}Dy – ^{162}Dy mixture, *Phys. Rev. A* **112**, 023317 (2025).

[72] C. Chin, R. Grimm, P. Julienne, and E. Tiesinga, Feshbach resonances in ultracold gases, *Rev. Mod. Phys.* **82**, 1225 (2010).

[73] S. K. Adhikari, Dynamically stable two- and four-droplet solitons in a very strongly dipolar NaCs condensate, *Phys. Rev. E* **111**, 054212 (2025).

[74] L. E. Young-S and S. K. Adhikari, Spontaneous dipolar Bose-Einstein condensation on the surface of a cylinder, *Phys. Rev. A* **108**, 053323 (2023).

[75] S. K. Adhikari, Hollow cylindrical droplets in a very strongly dipolar condensate, *Chaos, Solitons & Fractals* **199**, 116887 (2025).

[76] L. E. Young-S and S. K. Adhikari, Expansion dynamics of a cylindrical-shell-shaped strongly dipolar condensate, *Physica D* **465**, 134184 (2024).

[77] A. R. P. Lima and A. Pelster, Quantum fluctuations in dipolar Bose gases, *Phys. Rev. A* **84**, 041604 (2011).

[78] R. N. Bisset, R. M. Wilson, D. Baillie, and P. B. Blakie, Ground-state phase diagram of a dipolar condensate with quantum fluctuations, *Phys. Rev. A* **94**, 033619 (2016).

[79] S. Gupta, K. W. Murch, K. L. Moore, T. P. Purdy, and D. M. Stamper-Kurn, Bose-Einstein Condensation in a Circular Waveguide. *Phys. Rev. Lett.* **95**, 143201 (2005).

[80] C. Ryu, M. F. Andersen, P. Cladé, V. Natarajan, K. Helmerson, and W. D. Phillips, Observation of Persistent Flow of a Bose-Einstein Condensate in a Toroidal Trap, *Phys. Rev. Lett.* **99**, 260401 (2007).

[81] R. Kishor Kumar, L. E. Young-S., D. Vudragović, A. Balaž, P. Muruganandam, and S. K. Adhikari, Fortran and C programs for the time-dependent dipolar Gross-Pitaevskii equation in an anisotropic trap, *Comput. Phys. Commun.* **195**, 117 (2015).

[82] V. Lončar, L. E. Young-S., S. Škrbić, P. Muruganandam, S. K. Adhikari, and A. Balaž, OpenMP, OpenMP/MPI, and CUDA/MPI C programs for solving the time-dependent dipolar Gross-Pitaevskii equation, *Comput. Phys. Commun.* **209**, 190 (2016).

[83] L. E. Young-S. and S. K. Adhikari, Giant vortex in a harmonically-trapped rotating dipolar ^{164}Dy condensate, *Physica D* **475**, 134590 (2025).

[84] Y. Tang, A. Sykes, N. Q. Burdick, J. L. Bohn, and B. L. Lev, *s*-wave scattering lengths of the strongly dipolar bosons Dy^{162} and Dy^{164} , *Phys. Rev. A* **92**, 022703 (2015).

[85] V. I. Berezhiani, V. Skarka, and N. B. Aleksić, Dynamics of localized and nonlocalized optical vortex solitons in cubic-quintic nonlinear media, *Phys. Rev. E* **64**, 057601 (2001).

[86] D. Zajec and G. Wunner, Mean-field predictions for a dipolar Bose-Einstein condensate with ^{164}Dy , *Phys. Rev. A* **92**, 053609 (2015).

[87] H. Sakaguchi and B. A. Malomed, Solitons in combined linear and nonlinear lattice potentials, *Phys. Rev. A* **81**, 013624 (2010).

[88] N. G. Vakhitov and A. A. Kolokolov, Stationary solutions of the wave equation in a medium with nonlinearity saturation, *Radiophys. Quantum Electron.* **16**, 783–789 (1973); <https://doi.org/10.1007/BF01031343>.

[89] L. Bergé L., Wave collapse in physics: principles and applications to light and plasma waves, *Phys. Rep.* **303**, 259 (1998).